Improved Stability of a Grid-Following Converter Controller Supplying Virtual Inertia and Damping

Angelo Maurizio Brambilla, *Senior Member, IEEE*, Davide del Giudice, *Member, IEEE*, Federico Bizzarri, *Senior Member, IEEE*

***Abstract*—The share of converter-interfaced generator (CIG) units fuelled by renewables and scattered in distribution networks is increasing and causing the progressive phase out of synchronous generators and passive loads, which are the main source of vital parameters in ensuring frequency stability: inertia and load damping. To compensate the decreasing trend in these parameters, the control scheme of CIG units, typically of grid-following (GFL) kind, may include controls blocks that emulate the electro-mechanical behaviour of synchronous generators by letting them provide virtual inertia and load damping. However, a negative trait of GFL CIGs is that, contrary to grid-forming (GFM) CIGs (which are affected by other drawbacks), they rely on phase locked loops (PLLs). This dependency may trigger instability based on the strength of the grid and CIG operating conditions. In this paper, we propose a novel GFL CIG control scheme that emulates the electromechanical behaviour of synchronous generators better than conventional implementations. Eigenvalue and transient stability analyses of different power systems prove that, although the PLL model used is the same, the proposed GFL CIG control has a higher stability margin than its conventional counterpart, and provides a frequency support comparable with a synchronous generator of same inertia and load damping.**

***Index Terms*—Converter-interfaced generation, grid-following control, grid-forming control, phase locked loop, power system stability, frequency stability.**

I. INTRODUCTION

The transition from power generation dominated by synchronous generators to smart grids dominated by renewable-based distributed generation requires ensuring a reliable and adequate frequency support after disturbances. As thoroughly described in [1] and references therein, the progressive phase-out of synchronous generators and passive loads (and the stability services that come with those) can be compensated by acting on the control of converters used to interface the already installed generation and load units scattered in distribution feeders, hereafter referred to as converter-interfaced generators (CIGs).

Specifically, converter controls can be modified in an attempt to mimic the behaviour of synchronous generators replaced by CIGs by letting them provide virtual inertia and load damping [2], [3]. These ancillary services are mainly achieved by emulating with different approaches the

$$p^* - \left(\kappa_{\mathrm{si}} {}^{d\omega_g}\!/\!{}_{dt} + \kappa_{\mathrm{d}}\left(\omega_g - 1\right)\right) - p = 0 \tag{1}$$

swing equation modeling the electro-mechanical coupling of a synchronous generator. In (1), p^* [pu] (per unit) is the active power set-point of the CIG (which resembles the mechanical power from the prime mover in a synchronous generator), p [pu] is the electrical power, and ω_g [pu] is the angular virtual rotor speed. As to κ_{si} [s] and κ_{d} [pu], they are respectively the virtual inertia constant and load damping: the related term $\kappa_{\mathrm{si}} {}^{d\omega_g}\!/\!{}_{dt} + \kappa_{\mathrm{d}}\left(\omega_g - 1\right)$ corresponds to a power variation that adds to the CIG setpoint p^*. As in the classic swing equation of a synchronous generator, the inertia constant is related to the rate of change of frequency (ROCOF) ${}^{d\omega_g}\!/\!{}_{dt}$. On the contrary, the $\kappa_{\mathrm{d}}\left(\omega_g - 1\right)$ term in (1) implements a droop regulator that varies the CIG active power exchange proportionally to virtual rotor speed deviations. Hereafter, we refer to the κ_{d} parameter as load damping or, in short, simply as damping.

The derivation of ω_g varies with CIG implementation. To clarify this aspect, let us consider two classes of CIGs: grid-forming (GFM) and grid-following (GFL). In a GFM CIG, the ω_g virtual rotor angular speed of the synchronous generator is virtually emulated *internally* to the converter control (see [2], [4]–[7] for GFM CIG implementation examples based on virtual oscillator, droop control, and virtual synchronous generator). On the contrary, in a GFL CIG the ω_g term is derived by a phase locked loop (PLL) that tracks the *electrical frequency* at the point of common coupling (PCC) [8]. Thus, a GFM CIG does not need a PLL, while a GFL CIG heavily depends on it.

The reliance of GFL CIGs providing virtual inertia and damping on a PLL has a serious impact on their stability. For example, PLLs are known to be prone to instability in *weak* grids (i.e., where the voltage at the PCC varies strongly with power fluctuations, contrary to *strong* grids)[1] [9]. The work in [10] (and others following it [11]–[14]) identified that the reason for this instability lies in a closed loop at the PCC composed of the PLL and (1). In brief, the GFL CIG power exchange p given by (1) causes a phase variation at the PCC that drives the PLL, leading to a variation of the electrical frequency used to regulate the ω_g virtual rotor speed. In turn, changes in ω_g may trigger, based on (1), further variations in p. This vicious cycle may cause instability if the PLL is tuned inadequately. The amount and type of feedback (positive or

A.M. Brambilla and D. del Giudice are with Politecnico di Milano, DEIB, p.zza Leonardo da Vinci, no. 32, Milano, 20133, Italy. (e-mail: {angelo.brambilla,davide.delgiudice}@polimi.it).
F. Bizzarri is with Politecnico di Milano, DEIB, p.zza Leonardo da Vinci, no. 32, 20133 Milano, Italy and also with the Advanced Research Center on Electronic Systems for Information and Communication Technologies E. De Castro (ARCES), University of Bologna, 41026 Bologna, Italy. (e-mail: federico.bizzarri@polimi.it).

The work of F. Bizzarri was partially supported by Italian MUR under the grant PRIN 2022 DCNanoSyn, CUP D53D23001500006, project code 2022SPFP9R.

---

[1] A weak (strong) grid connection can be implemented by connecting the CIG to the grid through a long (short) line.

negative) heavily depend on the equivalent impedances shown by the GFL CIG at the PCC and that of the grid (which mirrors weak or strong grid connections).

It is easy to realize that a GFM CIG does not show this drawback as it does not use any PLL [15]. Based on the above, one may be inclined to adopt only GFM CIGs. However, such converters are not immune from stability issues, either [16]–[18]. Furthermore, as the grid-forming (GFM) name itself suggests, their purpose is to *form* the magnitude of the voltage at the PCC by forcing it through adequate power exchange. This holds also for converters of small domestic renewable power generation (e.g., few KVA) scattered in a distribution feeder. Such a control strategy can clash with the settings of the feeder substation and with other GFM CIGs forcing voltage magnitudes at very close adjacent PCCs in the same feeder. Under these circumstances, GFM CIGs may be compelled to exchange an amount of power too high to attain.

We show that the mechanism emulating the power exchange in a synchronous generator can be improved with respect to conventional, well known implementations [19]. Indeed, according to the swing equation, a synchronous generator varies its active power exchange following frequency deviations by acting on its rotor angle, that is, the phase difference between the internal generator of the synchronous generator model and the bus voltage. This intrinsically leads to a variation of also the exchanged reactive power. On the contrary, the p active power in (1) is almost always varied by acting on both the magnitude and phase of the voltage forced by the GFL CIG, leaving the reactive power unchanged [19].

To address this issue, we propose a GFL CIG control that better mimics the behaviour of a synchronous generator, and show that this makes a big difference in stability. Indeed, the previously mentioned stability issues that may arise by using a PLL are largely mitigated. To validate this statement, we first consider a simplified power grid comprising a GFL CIG connected to an infinite bus: through eigenvalue analyses we show how stability improves by shifting from a conventional to the proposed GFL CIG implementation, despite the PLL model used is the same. Then, to further support our claims, we perform eigenvalue and transient stability analyses in more complex networks and several scenarios, which consider (i) strong and weak grids connections by varying the length of the line through which a CIG is interfaced with the grid, and (ii) different CIG implementations (i.e., proposed and conventional GFL operating as voltage sources, GFL operating as current source, GFM, and a synchronous generator providing the same rated inertia and damping).

II. GFM CIG IMPLEMENTATION

Fig. 1(a) and (b-left side) depict the schematic of a synchronous generator and a voltage source converter (VSC) CIG, respectively. The latter is an average value model (AVM) of the VSC CIG: we selected this kind of model as it grants a CPU time to perform electromagnetic transient (EMT) simulations significantly lower than complete models that consider valve switching [20]. The model includes an output LC filter composed of r_F, l_F, and c_F. The dependent sources $u^*_{\{r,i\}}$ and i_{dc}, connected to the AC and DC side of the CIG, are such that the latter implements an ideal active power transfer, while the former is modulated for control purposes by exploiting as measurements $v_{\{r,i\},o}$, $i_{\{r,i\},o}$, and $i_{\{r,i\},CV}$. These variables, denoted by the r (real) and i (imaginary) indices, belong to the *global reference frame* and are used in the control scheme with their counterparts in the *local reference frame*, given by the d and q indices. The ri/dq and dq/ri transformation blocks in Fig. 1(c) convert one set of variables into the other, both related to Park's transform [21].

The blocks used to regulate the $u^*_{\{r,i\}}$ voltage of the controlled source vary with the CIG control. According to [22], power converters can be classified based on their control scheme into grid-forming (GFM), grid supporting (hereafter referred to as *grid following* – GFL), and grid feeding converters. Using a notation compatible with all the CIG control implementations available in the literature is a daunting if not impossible task. Therefore, we pick as reference implementation the GFM CIG shown in Fig. 5 of [8][2]. These controllers are detailed at high level in the following. To facilitate the presentation of other implementations in the next sections, we will re-use as much as possible the notation and control blocks adopted in that figure. We refer the reader to [8] when some details are omitted here to avoid redundancy: hereafter we focus mostly on the aspects that are worth mentioning to grasp the working principle of the GFL CIG control scheme we are proposing and its differences compared to a conventional one (operating either as voltage or current source), the GFM CIG, and a synchronous generator.

The GFM CIG control of [8] is also sketched in Fig. 1(d). Figure 1(c) shows the implementation of each of its control blocks except for *p/q control* block, whose equations are

$$\begin{cases} \kappa_{\text{si}} \dfrac{d\omega_{\text{VSM}}}{dt} = p^* - \widehat{p} - \kappa_{\text{d}} \left(\omega_{\text{VSM}} - 1 \right) \\ V_{\text{VSM}} = V^*_{\text{VSM}} + \kappa_{\text{q}} \left(q^* - \widehat{q} \right) \ , \end{cases} \tag{2}$$

where $\widehat{p}$ and $\widehat{q}$ are the low-pass filtered counterparts of the active/reactive power p/q, while p^*/q^* are the corresponding set-points of the CIG. The purpose of this block is to define the voltage V_{VSM} and angular speed variation ω_{VSM} of the voltage source emulated by the GFM CIG. V_{VSM} is determined through reactive power control: in particular, V^*_{VSM} is the set-point of V_{VSM} computed at power flow (PF)[3]. On the contrary, ω_{VSM} is governed by the swing equation: as stated in the Introduction, κ_{si} [s] and κ_{d} [pu] are respectively the virtual inertia constant and load damping. Note that, contrary to the case of GFL CIGs, here ω_{VSM} and the angle θ_{VSM} (i.e., its integral, used also in the *ri/dq* and *dq/ri* transforms) are generated *internally* to the converter control without relying on a PLL.

The voltage $V_{\text{VSM}} e^{\mathrm{j}\theta_{\text{VSM}}}$ is converted into rectangular coordinates $v^{**}_{\{d,q\}}$ and used as input by the *virtual impedance control* block, which consists in a lossless circuit-oriented control concept [24], [25]: by acting on the voltage generated

---

[2] In [8], the GFM CIG is referred to as virtual synchronous machine – controllers were borrowed from similar ones in [23].

[3] In other words, at power flow $V_{\text{VSM}} = V^*_{\text{VSM}}$, meaning that the CIG exchanges exactly q^*. A similar reasoning applies to other variables computed at PF and shown in the following.

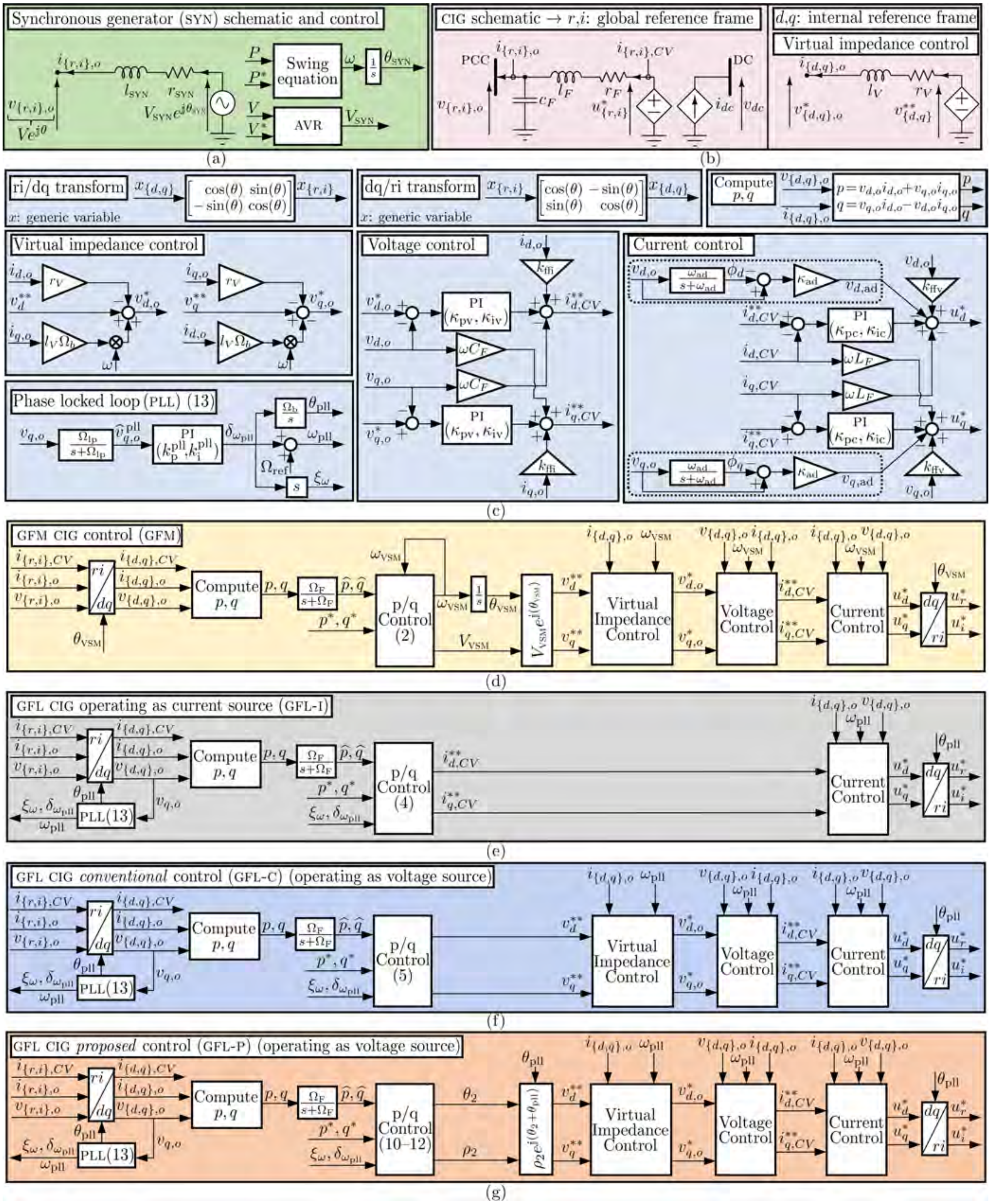

(a) (b) (c) (d) (e) (f) (g)

Fig. 1. Synchronous generator, CIG schematics and control schemes. Synchronous generator schematic and control scheme (a) — for simplicity, only the swing equation and the AVR (automatic voltage regulator) are included among the controls (although others may be added, such as the turbine governor). General average value model (AVM) CIG schematic in the global reference frame (left side) (the non linear controlled current source implements an ideal active-power transfer, that is, $i_{dc}v_{dc}+u_r^*i_{r,CV}+u_i^*i_{i,CV}=0$) and virtual impedance control in the internal reference frame (right side) (b). Control blocks used in different CIG implementations (c): *ri/dq* and *dq/ri* transform, *p/q* computation, *phase locked loop (*PLL*)*, *virtual impedance control, voltage control, and current control* (the dashed area collects the elements in charge of *active damping* [8]). GFM CIG (GFM) control scheme (d). Control scheme of a GFL CIG operating as a current source (GFL-I) (e). Conventional GFL CIG (GFL-C) control scheme (f). Proposed GFL CIG (GFL-P) control scheme (g). In (f) and (g), the CIG operates as a voltage source. For each implementation in (d-g), the *p/q control* block is described by equations reported in the main text. As to the PLL used in (e)-(g), its model is shown in (13) and described in Appendix A. Further details on the implementation of the other blocks in (c) can be found in [8]. Table II in Appendix B reports the parameters used in all the CIG implementations (d-g).

by the CIG at the PCC, it *virtually* emulates the circuit on the right side of Fig. 1(b): a synchronous generator viewed as a *voltage source behind an impedance*. This circuit is analogous to that of the *real* synchronous generator in Fig. 1(a). As the name suggests, this control emulates a virtual impedance. This can be done for different reasons, such as (i) modulate the impedance to vary the CIG contribution to faults [26], and (ii) implement a mostly inductive impedance in networks where the resistances are of the same order of magnitude as inductances (e.g., MV/LV networks) to achieve decoupled control of active and reactive power [8]. In any case, the *virtual impedance control* block adds another degree of freedom: as shown in the following, this feature is exploited in our proposed GFL CIG implementation to better replicate the behaviour of a synchronous generator during power disturbances.

The equations of the virtual impedance control in [8] – and replicated by the homologous block in Fig. 1(c) – are

$$\left\{ \begin{array}{l} v_{d,o}^{*} = v_{d}^{**} - r_V i_{d,o} + l_V \Omega_b \omega i_{q,o} \\ v_{q,o}^{*} = v_{q}^{**} - r_V i_{q,o} - l_V \Omega_b \omega i_{d,o} \ , \end{array} \right. \tag{3}$$

where $\omega\,[\mathrm{pu}]$ is the grid frequency estimate at the PCC[4], Ω_b is the base angular frequency (e.g., $2\pi 50$ or $2\pi 60\,\mathrm{rad/s}$), and r_V and $l_V \Omega_b \omega$ emulate the virtual impedance. $v_{\{d,q\}}^{**}$ (inputs) are the voltage set-points given by the active/reactive power control[5], while $v_{\{d,q\},o}^{*}$ (outputs) are the reference voltage values in the internal reference frame at the PCC of the CIG.

These values are translated into the $i_{\{d,q\},CV}^{**}$ reference currents by the *voltage control* block. Then, the *current control* block converts $i_{\{d,q\},CV}^{**}$ into the $u_{\{d,q\}}^{*}$ reference values, which are finally transformed by the dq/ri transform into the $u_{\{r,i\}}^{*}$ pair of voltages of the controlled source in Fig. 1(b).

III. PROVISION OF VIRTUAL INERTIA AND LOAD DAMPING WITH GFL CIGS

GFL CIGs can operate as current or voltage sources [22]. When working as current sources (GFL-I), they can be controlled as in Fig. 1(e). The *p/q control* block model is

$$\left\{ \begin{array}{l} \varepsilon_d = p^* - \left(\kappa_{\mathrm{si}}\xi_\omega + \kappa_{\mathrm{d}}\delta_{\omega_{\mathrm{pll}}}\right) - \widehat{p} \\ i_{d,CV}^{**} = i_{d,CV}^{*} + \kappa_{pp}\varepsilon_d + \displaystyle\int \kappa_{ip}\varepsilon_d dt \\ \varepsilon_q = q^* - \widehat{q} \\ i_{q,CV}^{**} = i_{q,CV}^{*} + \kappa_{pp}\varepsilon_q + \displaystyle\int \kappa_{ip}\varepsilon_q dt \ , \end{array} \right. \tag{4}$$

where the errors $\varepsilon_{\{d,q\}}$ drive the PI regulators of κ_{pp} and κ_{pi} gains, while $i_{\{d,q\},CV}^{*}$ are the set-points of $i_{\{d,q\},CV}^{**}$ computed at PF. The first equation in (4) allows frequency ancillary services provision (i.e., virtual inertia κ_{si} and damping κ_{d}) through the CIG[6]. The p^* active power is assumed positive when generated: the $\left(\kappa_{\mathrm{si}}\xi_\omega + \kappa_{\mathrm{d}}\delta_{\omega_{\mathrm{pll}}}\right)$ term lowers the amount of injected active power when the $\delta_{\omega_{\mathrm{pll}}}$ angular frequency increases and/or the ξ_ω ROCOF is positive.

This implementation (similar to that shown in Fig.1 of [27]) has two main differences with respect to that in Fig. 1(d). First, the *p/q control* block outputs reference values of $i_{\{d,q\},CV}^{**}$ instead of $v_{\{d,q\}}^{**}$, thus lacking the *virtual impedance control* and *voltage control* blocks. Second, the *p/q control* block emulates the virtual inertia and damping provision by exploiting the ξ_ω ROCOF and the $\delta_{\omega_{\mathrm{pll}}}$ angular frequency estimated by the PLL model in (13), shown in Fig. 1(c) and described in Appendix A. On the contrary, GFM CIGs do not rely on a PLL.

Alternatively, GFL CIGs may also operate as voltage sources behind (virtual) impedances to obtain the desired forcing currents. Figure 1(f) and (g) depict possible control implementations of the CIG in these cases, which are respectively referred to as conventional (GFL-C) and proposed (GFL-P) GFL CIG control. By comparing Fig. 1(d-g), the GFL-C and GFL-P control schemas are more similar to that of the GFM CIG and more complex than their GFL-I counterpart. This gain in complexity comes with the advantage that GFL CIGs acting as voltage sources can operate in both grid-connected and island mode by properly switching the type of outer controller [22].

The next subsections outline the differences between the GFL-C and GFL-P implementations, both in terms of controls and features observed when carrying out stability analyses. We are mostly interested in these implementations because any difference in terms of stability properties with respect to GFM CIGs can be only ascribed to the presence of the PLL and the equations of the *p/q control* block. On the contrary, in the case of a GFL-I CIG, also the absence of the *virtual impedance control* and *voltage control* blocks may affect the stability properties of the CIG.

A. Conventional GFL CIG *implementation (*GFL-C*)*

The GFL-C CIG implementation is depicted in Fig. 1(f). In this case, the equations of the *p/q control* block are

$$\left\{ \begin{array}{l} v_{d}^{**} = v_{d}^{*} + \kappa_{\mathrm{p}}\left(p^* - \left(\kappa_{\mathrm{si}}\xi_\omega + \kappa_{\mathrm{d}}\delta_{\omega_{\mathrm{pll}}}\right) - \widehat{p}\right) \\ v_{q}^{**} = v_{q}^{*} + \kappa_{\mathrm{q}}\left(q^* - \widehat{q}\right) \ . \end{array} \right. \tag{5}$$

As its GFL-I counterpart, this implementation controls p and q separately. The $\widehat{p}$ and $\widehat{q}$ filtered powers drive the controllers of κ_{p} and κ_{q} gains in (5), where $v_{\{d,q\}}^{*}$ are the set-points of $v_{\{d,q\},o}^{*}$ computed at PF. The provision of ancillary services is analogous to that of the GFL-I CIG, as it still relies on the PLL. The rest of the control scheme is the same of Fig. 1(d).

To study the stability properties of this implementation, we first perform eigenvalue analyses of the simplified power grid in Fig. 2, which includes an infinite bus of $E_{\{r,i\}}$ voltage and a CIG connected through a line described by an RLC circuit (which models the impedance "seen" by the CIG at the PCC).

---

[4] In the equations and corresponding block implementation, ω is without a subscript to refer to the most general case possible. The same applies for the θ variable in the ri/dq and dq/ri blocks in Fig. 1(c). When dealing with a GFM (GFL) CIG, $\omega = \omega_{\mathrm{VSM}}$ ($\omega = \omega_{\mathrm{PLL}}$) and $\theta = \theta_{\mathrm{VSM}}$ ($\theta = \theta_{\mathrm{PLL}}$).

[5] In other words, $v_{\{d,q\}}^{**}$ are such that at power flow the $v_{\{d,q\},o}^{*}$ reference voltages at the PCC ensure the desired p/q exchange. In [8], $v_d^{**} \equiv v^{**}$ and $v_q^{**} = 0$. Here, however, we used a different setting to make the virtual impedance control compatible with multiple implementations shown later.

[6] Note that this implementation leaves the *reactive power equation unchanged* (third equation in (4)). In principle, this equation may be modified to let the CIG react to voltage variations, too. Moreover, if $\kappa_{\mathrm{si}} = \kappa_{\mathrm{d}} = 0$, no ancillary services are provided, and the GFL CIG emulates a PQ-load (i.e., a constant power load exchanging p^* and q^*). According to [22], in this case the CIG control becomes that of a simple *grid-feeding* converter.

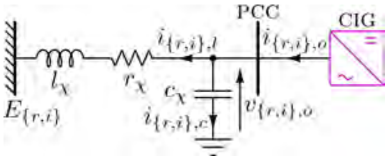

Fig. 2. The schematic of the simplified power grid. $E_{\{r,i\}}$ implements an infinite bus connected to the CIG through a line given by an *RLC* equivalent circuit in the *dq*-frame, which can be algebraic or dynamic. System data: $l_0 = 0.2526\,\mathrm{mH/km}$, $c_0 = 0.1837\,\mathrm{\mu F/km}$, $r_0 = 84.3\,\mathrm{m\Omega/km}$, $E_r = 145\,\mathrm{kV}$, $E_i = 0\,\mathrm{kV}$, $\Omega_b = 100\pi$, $\kappa_\mathrm{d} = 100\,\mathrm{M}$, $\kappa_\mathrm{si} = 0.5\,\mathrm{M}$. The line model, whose nominal length is 200 km, coincides with that in [28] (paragraph 6.4.1). The same line model was used also in [29].

While doing this analysis, we resort to the equivalent linear model of the GFL-C CIG with (5) computed at the PF and assume that the other controls blocks (e.g., *voltage control* and *current control*) in Fig. 1(c) are so much faster with respect to the *p/q control* one that their response can be considered as *immediate* (i.e., their band-width is assumed infinite). This common simplification, justified by the fact that the electromechanical grid dynamics are relatively slower, is such that the current injected by the GFL-C CIG is

$$i_{\{r,i\},o} = \frac{\left(p^* - \left(\kappa_\mathrm{si}\xi_\omega + \kappa_\mathrm{d}\delta_{\omega_\mathrm{pll}}\right)\right) v_{\{r,i\},o} \pm q^* v_{\{i,r\},o}}{v_{r,o}^2 + v_{i,o}^2} \,. \quad (6)$$

While performing eigenvalue analyses, we use either an algebraic or a dynamic model of the *RLC* circuit representing the line [30]. The *dynamic* model of the simplified grid we use is

$$\begin{cases} v_{\{r,i\},o} = l_\chi \dfrac{di_{\{r,i\},l}}{dt} + r_\chi i_{\{r,i\},l} \mp \Omega_b l_\chi i_{\{i,r\},l} + E_r \\ i_{\{r,i\},c} = c_\chi \dfrac{dv_{\{r,i\},o}}{dt} \mp \Omega_b c_\chi v_{\{i,r\},o} \\ i_{\{r,i\},l} = i_{\{r,i\},o} - i_{\{r,i\},c} \,. \end{cases} \quad (7)$$

In the equations, $l_\chi = \chi l_0$, $c_\chi = \chi c_0$, and $r_\chi = \chi r_0$, where χ mirrors the line relative length (the nominal value of χ is 1). Contrary to its dynamic counterpart, the *algebraic* model neglects the time derivatives in (7). This latter model is usually adopted in RMS transient stability analyses in the *dq*-frame to increase simulation efficiency [2], [7], but can lead to erroneous results [31]. In particular, as shown shortly, we exploit this analysis to show how using algebraic or dynamic line models can make a deep difference on the results of the eigenvalue analyses and, thus, stability.

The full *non-linear* model we consider includes equations (6) (GFL-C CIG supplying synthetic inertia and damping), (7) (power grid), and (13) (PLL). We study its small-signal stability through eigenvalues analyses by varying the χ relative length of the line connecting the CIG to the infinite bus.

Firstly, we compute the PF solution assuming that at steady-state $p^* = q^* = 0$ and the line is described by the algebraic model. In this case, the *only dynamics* are contributed by the PLL, which includes three state variables (i.e., $\widehat{v}_{q,o}^{\mathrm{pll}}$, $\delta_{\omega_\mathrm{pll}}$, and θ_pll). Thus, the resulting small-signal linear model includes just as many eigenvalues. Figure 3 shows how the real part of the eigenvalues $\lambda_{1,2,3}$ changes with χ (x-axis). The **black** traces refer to eigenvalues with negative real part and the **red** ones to those with positive real part (i.e., unstable behaviour). As shown, instability arises with a sufficiently long line. This is coherent with what was mentioned in the Introduction: the PLL (i.e., the only component introducing dynamics in this case) is prone to cause instability in weak grids, which are mirrored by GFL CIGs connected with long lines.

We now repeat the same eigenvalue analysis by using the dynamic model of the line, which adds, as can be inferred from (7), four more state variables (i.e., $i_{\{r,i\},l}$ and $v_{\{r,i\},o}$). The resulting seven eigenvalues are shown in Fig. 4. Compared to

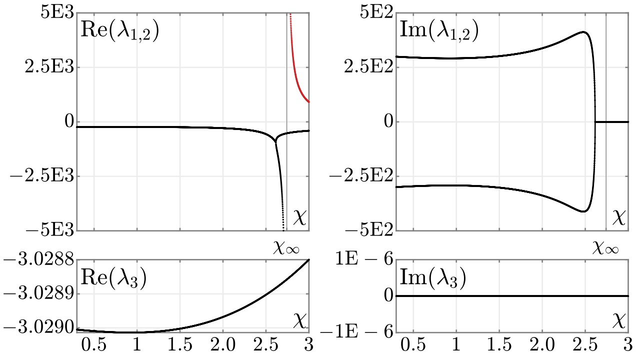

Fig. 3. The real and the imaginary parts of the λ_k ($k \in \{1, \ldots, 3\}$) eigenvalues as a function of χ (x-axis), which scales the nominal line length. Eigenvalues are computed by considering the grid in Fig. 2, by using the *conventional* GFL CIG model (GFL-C), and representing the line connecting the CIG to the infinite bus through an *algebraic* model. The trace color in the left panels becomes **red** when the real part of an eigenvalue is positive (unstable). In the upper-left panel is it possible to notice that, at $\chi = \chi_\infty$ there is a vertical asymptote, since one of the dynamic variables of the system becomes algebraic. One real eigenvalue goes to $\pm\infty$ for $\chi \rightarrow \chi_\infty^\pm$.

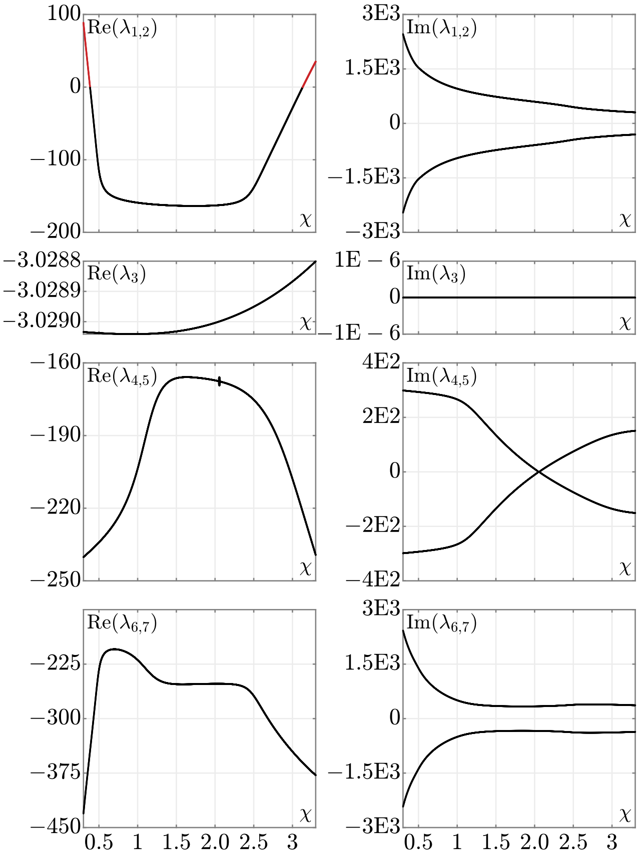

Fig. 4. The real and the imaginary part of the λ_k ($k \in \{1, \ldots, 7\}$) eigenvalues depicted as a function of relative line length χ. Compared to Fig. 3, the shown results are still obtained with the *conventional* GFL CIG model (GFL-C), but by using a *dynamic* line model instead. The trace color in the left panels becomes **red** when the real part of an eigenvalue is positive (unstable).

Fig. 3, instability arises not only for long lines, but also for short ones (i.e., strong grids).

We conducted further analyses on the last case study involving the dynamic line model. For space reasons, we do not show the results here. In brief, we observed that, by varying the line length, the instability interval on the left side of the plot in Fig. 4 widens. In principle, one can think of counteracting this phenomenon by adjusting the PLL parameters to avoid instability both for short and long line lengths. Unfortunately, as discussed for instance in [29][7], there is yet no way of finding values of the $\kappa_{\mathrm{p}}^{\mathrm{pll}}$, $\kappa_{\mathrm{i}}^{\mathrm{pll}}$ gains of the PLL that ensure stability in a good range of line lengths in spite of variations in grid strength and system operating conditions over time.

B. Proposed GFL CIG *implementation (*GFL-P*)*

The proposed GFL (GFL-P) CIG control implementing virtual inertia and damping, shown in Fig. 1(g), is inspired by the behaviour of the synchronous generator in Fig. 1(a) after a frequency disturbance (e.g., due to a load step-change). In these cases, the synchronous generator reacts by varying its rotor angle θ_{SYN} with respect to the voltage phase at the PCC, without altering its open circuit voltage V_{SYN}. This behaviour is such that, right after a frequency disturbance, the voltage across the machine impedance $r_{\text{SYN}}+\mathbb{j}\omega l_{\text{SYN}}$ varies and both its active and reactive power exchange vary.

To provide ancillary services with the GFL-P CIG, we emulate the behaviour of the synchronous machine described above by exploiting the *virtual impedance control*. To detail this, consider its schematic shown in the right side of Fig. 1(b), through which the $i_{d,o}+\mathbb{j}i_{q,o}$ current can be derived as

$$i_{d,o}+\mathbb{j}\,i_{q,o}=\frac{\rho_2 e^{\mathbb{j}(\theta_{\mathrm{pll}}+\theta_2)}-\rho_1 e^{\mathbb{j}\theta_{\mathrm{pll}}}}{r_V+\mathbb{j}x_V} \tag{8}$$

where $\rho_1=\sqrt{(v_{d,o}^{*})^2+(v_{q,o}^{*})^2}$, $\rho_2=\sqrt{(v_d^{**})^2+(v_q^{**})^2}$, $\tan(\theta_2)={}^{v_q^{**}}\!/_{v_d^{**}}$, while r_V and $x_V=\Omega_b\omega_{\mathrm{pll}}l_V$ make up the virtual impedance. In the schematic, the $\rho_1 e^{\mathbb{j}\theta_{\mathrm{pll}}}$ term is the voltage at the PCC in the internal reference frame, which is at one end of the virtual impedance, while $\rho_2 e^{\mathbb{j}(\theta_{\mathrm{pll}}+\theta_2)}$ is the voltage at the other end. The resulting current in (8) is what the GFL-P CIG has to provide by acting on θ_2.

The p active and q reactive power exchange at the PCC are

$$p+\mathbb{j}q=\rho_1 e^{\mathbb{j}\theta_{\mathrm{pll}}}\overline{\left(\frac{\rho_2 e^{\mathbb{j}(\theta_{\mathrm{pll}}+\theta_2)}-\rho_1 e^{\mathbb{j}\theta_{\mathrm{pll}}}}{r_V+\mathbb{j}x_V}\right)}$$

where the $\overline{}$ over-line notation stands for the complex conjugation operator. It follows that the active power is

$$p=\frac{r_V}{r_V^2+x_V^2}\left(\rho_1\rho_2\cos(\theta_2)-\rho_1^2\right)+\frac{x_V}{r_V^2+x_V^2}\rho_1\rho_2\sin(\theta_2) \tag{9}$$

which is a non-linear implicit algebraic function of θ_2.

While in the GFL-C CIG implementation the outputs of the *p/q control* are the voltages $v_{\{d,q\}}^{**}$, in the proposed one they are replaced by the voltage phase θ_2 and amplitude ρ_2.

The virtual rotor angle θ_2 is computed by first deriving the

$$p^{**}=p^{*}+\kappa_{\mathrm{p}}\left(p^{*}-\left(\kappa_{\mathrm{si}}\xi_\omega+\kappa_{\mathrm{d}}\delta_{\omega_{\mathrm{pll}}}\right)-\widehat{p}\right) \tag{10}$$

updated active power set-point p^{**} that, compared to p^{*}, includes virtual inertia and damping provision (recall that $\widehat{p}$ and $\widehat{q}$ are the low-pass *filtered* active and reactive power). Similarly to (5), inertia and damping supply depend on the ξ_ω (ROCOF) and the $\delta_{\omega_{\mathrm{pll}}}$ variation of the electrical frequency at the PCC, respectively, both derived by the PLL. In (10), the p^{*} active power is assumed positive when generated. The $\left(\kappa_{\mathrm{si}}\xi_\omega+\kappa_{\mathrm{d}}\delta_{\omega_{\mathrm{pll}}}\right)$ contribution by the ancillary service lowers the amount of injected active power when the $\delta_{\omega_{\mathrm{pll}}}$ angular frequency tracked by the PLL increases and/or the ξ_ω ROCOF is positive (positive frequency derivative). By setting $p=p^{**}$, (9) is solved with respect to θ_2 as[8]

$$\begin{cases}\theta_2=2\,\mathrm{atan}\left(\dfrac{x_V-\sqrt{\Delta}}{\Gamma+r_V}\right)\\ \Delta=r_V^2+x_V^2-\Gamma^2\\ \Gamma=p^{**}\dfrac{r_V^2+x_V^2}{\rho_1\rho_2}+\dfrac{r_V\rho_1}{\rho_2}\end{cases}. \tag{11}$$

This control logic is such that, right after a power disturbance triggers frequency deviations, the $\left(\kappa_{\mathrm{si}}\xi_\omega+\kappa_{\mathrm{d}}\delta_{\omega_{\mathrm{pll}}}\right)$ term in (10) alters p^{**}, which we equate to p in (9). As shown by (11), θ_2 varies accordingly and so doing, q varies too, as happens in a synchronous machine. Thus, in GFL-P CIG a variation of the p exchanged active power leads to a related variation of the q exchanged reactive power. This feature is in opposition to the GFL-C CIG implementation described in Section III-A, where p and q are controlled separately. Indeed, by observing (5), we see that $\left(\kappa_{\mathrm{si}}\xi_\omega+\kappa_{\mathrm{d}}\delta_{\omega_{\mathrm{pll}}}\right)$ exclusively acts on v_d^{**} and not on v_q^{**}; this means that GFL-C CIG varies only the exchanged active power and not the reactive power.

As to the ρ_2 voltage magnitude of the voltage source behind the virtual impedance, it can be regulated to control the reactive power exchange as

$$\rho_2=\rho_2^{*}+\kappa_{\mathrm{q}}\left(q^{*}-\widehat{q}\right)\ , \tag{12}$$

where the q^{*} set-point and κ_{q} gain are the same used in (5), $\widehat{q}$ is the low-pass filtered version of the measured q reactive power, while ρ_2^{*} is the voltage magnitude set-point that ensures the CIG exchanges $q=q^{*}$ at PF. Note that the ρ_2 magnitude in (8) does not vary if θ_2 does: variations of ρ_2 are exclusively due to the reactive power controller (12).

Therefore, the *virtual impedance control* uses as input $v_d^{**}+\mathbb{j}v_q^{**}=\rho_2 e^{\mathbb{j}(\theta_2+\theta_{\mathrm{pll}})}$. The rest of the control scheme in Fig. 1(g) (given by the *virtual impedance*, *voltage*, and *current control*) is analogous to that in Fig. 1(d) and explained before.

To show the improved stability of a GFL-P CIG compared to a GFL-C one, we repeated the same eigenvalue analysis of Section III-A on the grid in Fig. 2 by exclusively using a

---

[7] Ref. [29] mainly considers low-voltage ride-through events but also large power imbalances in a simple test system; [9], [32] consider a large set of real world events where PLL were to blame for system instability if for example grid configurations change due to a generation loss or line switching.

[8] Given the square root of Δ and the possible singularity in the denominator in the first row of (11), we limited Γ in the $-\eta r_V\leq\Gamma\leq\eta\sqrt{r_V^2+x_V^2}$ interval (in our case $\eta=0.99$). This mathematical ploy ensures a real solution is always found and does not alter the general operating principle of the GFL-P CIG. In deriving θ_2, we once more exploit the assumption of infinite bandwidth for the inner control loops.

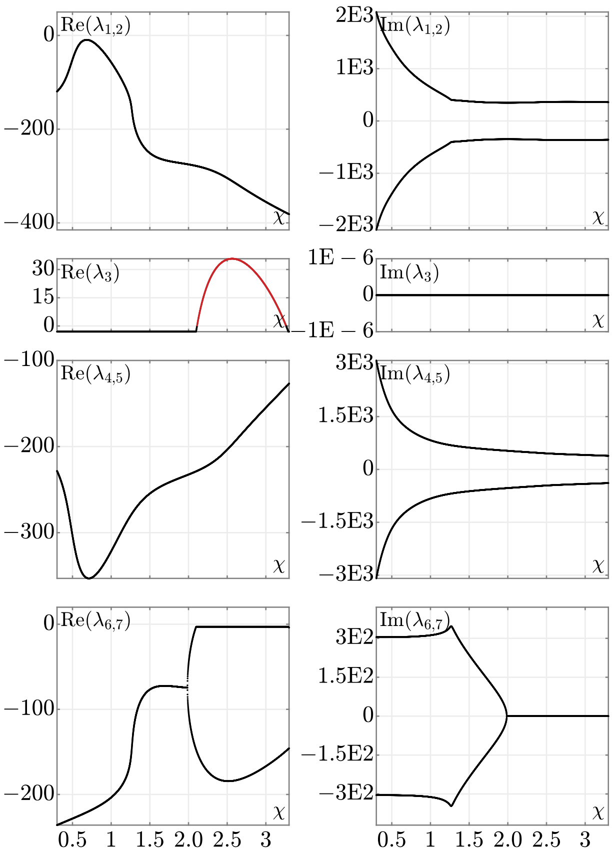

Fig. 5. The the real and the imaginary parts of the λ_k ($k \in \{1,...,7\}$) eigenvalues depicted as a function of relative line length χ. Compared to Fig. 4, the results shown are obtained with the *proposed* GFL CIG model (GFL-P) and a *dynamic* line model (traces share the same color code).

dynamic line model (the algebraic model was not used due to its previously mentioned inaccuracy) and the GFL-P CIG model. We assume again that the CIG control blocks on the right of the *p/q control* one in Fig. 1(g) have infinite bandwidth with respect to the relatively slower process of power system frequency regulation. Thus, in our analyses the equations of the proposed controller are purely algebraic.

Figure 5 depicts how the real parts of the seven eigenvalues computed at PF in this case evolve with the χ line length scaling factor. When the GFL-P CIG is used, the system is stable for any line length up to more than twice its nominal value. Thus, with this implementation there is a *unique set* of PLL parameter values that ensures stability in a wide range of line lengths starting from an extremely strong up to a weak grid connection. This is in contrast with the GFL-C (and possibly GFM) CIG implementation, which exhibited instability also with strong grid connections (i.e., short lines).

IV. DISCUSSION

We now focus more on Fig. 1 to identify and recap the main differences in terms of control among a synchronous generator (a), a GFM CIG (d), a conventional GFL CIG (GFL-C) (f), and our proposed GFL CIG (GFL-P) (g).

Starting from the synchronous generator, it is known that the swing equation describes its behaviour after a power mismatch, which causes a deviation in system frequency and, in turn, in its angular speed ω_{SYN} and rotor angle θ_{SYN}. On the contrary, the open-circuit voltage amplitude V_{SYN} is typically regulated through an automatic voltage regulator, which ensures a given voltage at the PCC of the machine (alternatively, reactive power exchange may be regulated, instead).

The GFM CIG can replicate this behaviour through the *p/q control* block, which outputs the voltage magnitude V_{VSM} and phase θ_{VSM} of the voltage source emulated by the virtual impedance block in the right side of Fig. 1(b) [5], [8]. These variables are the counterparts of V_{SYN} and θ_{SYN} for a synchronous generator. It is also worth reminding that, in this case, the virtual rotor speed is not estimated by a PLL, but rather generated *internally* by mimicking the swing equation.

However, as stated in the Introduction, a major drawback of GFM CIGs is that they must *form* the PCC voltage magnitude voltage at the PCC — which may not always be possible or practical and that can be affected by "other" stability problems with respect to GFLs [16]–[18]. This issue does not arise with GFL-C CIGs, which, however, are prone to stability issues due to their reliance on a PLL to estimate the angular speed. Moreover, their *p/q control* block outputs directly voltage set-points in the d and q-axis (i.e., v_d^{**} and v_q^{**}), rather than a voltage magnitude and angle.

By looking at all the implementations, the GFL-P shown in Fig. 1(g) is somewhat of an hybrid between the previously mentioned CIG control implementations. Just like GFL-C CIGs, it relies on a PLL to implement the swing equation in (10): in other words, ancillary services are supplied without using any internal independent frequency/phase reference. However, the equations embedded in the *p/q control* block in the GFL-C and GFL-P case follow a different logic. Indeed, analogously to GFM CIGs, the *p/q control* block of GFL-P CIGs outputs a voltage magnitude ρ_2 and angle θ_2 (which is later converted in d and q-axis voltage components and fed to the *virtual impedance control*). In particular, the GFL-P control scheme is such that only the angle θ_2 must change after an active power mismatch, as it happens in a synchronous generator. As shown in the next section, this hybrid form grants GFL-P CIGs higher stability than those of GFL-C (and also of GFL-I) kind, while retaining satisfactory virtual inertia and damping provision.

V. NUMERICAL SIMULATIONS

We show hereafter the results obtained by analysing two power systems[9]. Each of them is simulated by considering one CIG connected at different buses (mirroring weak and strong grid connections) and five scenarios: GFL-I, GFL-C, GFL-P, GFM, and SYN (i.e., the same labels used in Fig. 1). In each case, the CIG is respectively controlled as a GFL working as current source, a conventional or proposed GFL working as voltage source, a GFM, or replaced by a synchronous generator. These scenarios highlight two aspects: (i) the GFL-P CIG has an improved stability compared to its GFL-I and GFL-C counterparts, and (ii) its virtual inertia and damping provision properly emulates that of a synchronous generator.

---

[9] We run all simulations with the simulator PAN [33]–[35], on an Intel® Xeon® Gold-6238R-CPU@2.20 GHz, Linux Mint 20.1 computer.

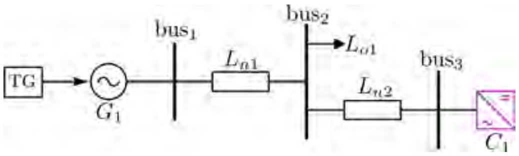

Fig. 6. The schematic of the simple power system used to show that stability depends on where C_1 CIG is connected and its control. In the figure, the CIG is connected at bus_3, but we also assessed system stability when it is connected at bus_1 and bus_2. The G_1 synchronous generator is equipped with a TG turbine governor. The parameters of the grid components are the following (parameters lacking unit of measure are in [pu]). G_1: order 6, $p_{\mathrm{rating}}=6\,\mathrm{MVAR}$, $v_{\mathrm{rating}}=69\mathrm{kV}$, $x_l=0$, $r_a=3\mathrm{m}$, $x_d=1$, $x_d'=0.185$, $x_d''=0.13$, $t_{d0}'=6$, $t_{d0}''=40\mathrm{m}$, $x_q=0.98$, $x_q'=0.36$, $x_q''=0.13$, $t_{q0}'=0.3$, $t_{q0}''=0.099$, $h=10$, $d=2$. TG: type 1, $r=0.02$, $t_s=0$, $t_c=1\mathrm{m}$, $t_3=0$, $t_4=0$, $t_5=50$. L_{n1}: $r=0.056$, $x=0.973$, $b=0.340\mu$, $p_{\mathrm{rating}}=10\,\mathrm{MVAR}$, $v_{\mathrm{rating}}=69\mathrm{kV}$. L_{n2}: $r=1.56\chi$, $x=1.973\chi$, $b=0.340\mu\chi$, $p_{\mathrm{rating}}=10\,\mathrm{MVAR}$, $v_{\mathrm{rating}}=69\mathrm{kV}$. L_{o1}: $p_c=0.07$, $q_c=0.01$, $p_{\mathrm{rating}}=100\,\mathrm{MVAR}$, $v_{\mathrm{rating}}=69\mathrm{kV}$. The detailed description of these parameters can be found in [36]. When the C_1 CIG is of GFL-I, GFL-C, GFL-P or GFM kind, its parameters are the same as those in Table II, except for $V_{\mathrm{ref}}=69\,\mathrm{kV}$, $P_{\mathrm{ref}}=1\,\mathrm{M}$, $\kappa_{\mathrm{si}}=100$, and $\kappa_{\mathrm{d}}=100$.

Unless otherwise stated, when the CIG is of GFL-I, GFL-C, GFL-P or GFM kind, the parameters in Table II of Appendix B are used. Lastly, when replacing the CIG with a synchronous generator, we use the classical model of order 2 shown in Fig. 1(a) (i.e., a constant generator behind an impedance [21]). Note that the GFM CIG and synchronous generator parameters are tuned so that they provide the same rated value of virtual inertia and damping of the GFL-I, GFL-C, and GFL-P CIGs.

A. A simple power system

The first power system is simple and with it in some way we replicate the analysis conducted for a similar target in [29] (i.e., the effects on system stability by connecting a GFL at different buses and with different system configurations). Its schematic is shown in Fig. 6: it includes the G_1 synchronous generator and the C_1 CIG. Other than simulating the four scenarios mentioned above, we analyze what changes by connecting the C_1 CIG at bus_1, bus_2, or bus_3. While doing so, we use both algebraic and dynamic models of lines, transformer and loads[10]. By looking at the schematic of this simple power system and the data in the caption of Fig. 6, the connections of C_1 CIG at bus_1 and bus_2 mirror a strong grid (notice that the generator has a relatively small impedance and the same holds also for the L_{n1} line), whereas that at bus_3 could mirror a strong or weak grid depending on the parameter χ used to vary the length of the L_{n2} line.

For each scenario and case considered, we performed an eigenvalue analysis at the PF and a transient stability analysis by simulating a -10% step variation of the active and reactive power of the L_{o1} load. Table I summarises the stability results obtained. The ✓and × marks respectively denote stable and unstable cases, while the '—' mark refers to cases that cannot be actually implemented: this happens when the C_1 CIG is of GFM kind and is supposed be connected in parallel to the G_1 synchronous generator at bus_1[11]. As shown, the grid is always stable if the L_{n1} and L_{n2} lines are modeled as algebraic elements (i.e., **Algebraic** column in Table I). On the contrary, instability may arise in some cases when the model of the lines is dynamic (**Dynamic** column). This highlights once again that, contrary to dynamic line models (whose use in RMS simulations in the dq-frame ensures the same accuracy of EMT ones [21]), algebraic line models may lead to misguided conclusions about system stability [31].

TABLE I
STABILITY IN DIFFERENT SIMULATION CASES (SIMPLE POWER SYSTEM)

	Algebraic			Dynamic				
	bus_1	bus_2	bus_3	bus_1	bus_2	bus_3		
						χ_1	χ_{30}	χ_{40}
SCR				30.35	22.70	13.81	1.07	0.81
GFL-I	✓	✓	✓	✓	×	×	×	×
GFL-C	✓	✓	✓	✓	✓	×	×	×
GFL-P	✓	✓	✓	✓	✓	✓	✓	×
GFM	—	✓	✓	—	✓	✓	×	×
SYN	✓	✓	✓	✓	✓	✓	✓	✓

As to the unstable cases, they mainly occur when the C_1 CIG is connected at bus_3. The χ_{30} and χ_{40} labels in Table I indicate that the length of L_{n2} is increased by 30 and 40 times[12], respectively (in the χ_1 case, the line length is the nominal one). When the CIG is of GFL-I or GFL-C kind and is connected at bus_3, the system is always unstable, regardless of the value of χ (in addition, when a GFL-I CIG is considered, instability arises also when the connection takes place at bus_2). On the contrary, if the CIG is of GFL-P kind, instability arises only in the χ_{40} case, which confirms the improved stability of the proposed GFL implementation compared to its conventional counterpart. It is also worth noting that the GFM scenario is already unstable in the χ_{30} case.

1) Discussion on stability properties: The results shown in Table I may lead one to ponder on the possible roots of instability in each case. Instability depends on a multitude of factors, including the parameters of the PLL (if the CIG uses it, depending on the implementation) [9], [10], [29], [32], of the other controls employed in the CIG, and of the lines that connect the C_1 CIG to the G_1 synchronous generator. In this context, a common metric used as indicator of possible stability issues is the so-called short-circuit ratio (SCR) [21]. According to Chapter 2 of [37], the SCR at a given bus k is defined as $S_{\mathrm{scr}} = {}^{S_{\mathrm{scmva}}}/_{P_{\mathrm{rmw}}}$, where S_{scmva} is the short-circuit MVA power at bus k *before* the connection of the new CIG at that same bus, while P_{rmw} is the rated MW active (DC) power of a *new connected* CIG (or, in general, of any AC/DC converter). As shown in [38], the higher the SCR, the higher the short-circuit current and the lower the impedance seen from the PCC of the CIG. In turn, a lower equivalent impedance implies that the voltage at the PCC is relatively stiff (i.e., it is only slightly affected by power fluctuations). This concept, which is tightly linked to the notion of *strong/weak grid connection*, is the reason why the SCR is usually used as an indicator to express the likelihood of issues related with, for instance, adverse CIG control interactions and voltage instability.

---

[10] The loads are dynamic RL equivalent circuits; the series inductances of transformers are dynamic elements.

[11] The GFM should force the voltage at the PCC and this may clash with the voltage set by the synchronous generator of large power capacity.

[12] These values may seem very high, but recall that χ scales the nominal length of the L_{n2} line, which is very short in our case.

However, it is argued that the adoption of the SCR in a system with a high share of CIGs may lead to misguided conclusions about its stability [38]. For instance, since the SCR is obtained by *static* studies (i.e., S_{scmva} is evaluated at the power flow solution at $50/60\,\text{Hz}$) and *before* the connection of the new CIG, it neglects (for better or worse) (i) intrinsic features (e.g., stability issues) of the new connected CIG and (ii) interactions among already connected CIGs and the main grid at other frequencies than $50/60\,\text{Hz}$. Thus, a different metric should be adopted for generic stability assessments in CIG-dominated grids — however, consensus has not been reached yet as to which is the right metric to actually use [37].

To prove that a high SCR does not always imply stability (not even in a grid with a single CIG), we reported in Table I the SCR obtained in each simulated case associated with the **Dynamic** column. As expected, the SCR changes with the bus where the CIG is connected and, when the connection to bus_3 is considered, with the L_{n2} line length scaling factor χ. In some cases, the SCR is very high (much more than the minimum value of 3 generally attributed to *strong* grids [38])[13], but instability still occurs. For instance, in the χ_1 case, instability arises when the CIG is of GFL-I or GFL-C kind but not with the other implementations, although the SCR is the same (i.e., 13.81).

What stated so far shows that the SCR is a very rough (if not unreliable) (in)stability indicator, but does not explain why stability results change with the CIG implementation. Based on the control schemes depicted in Fig. 1, the results in Table I, and further analyses carried out in the simulated cases (not shown here for brevity), the following holds.

- The GFL-I CIG is stable in less cases than the other implementations because it lacks the *virtual impedance block*. All the CIGs we used display a *negative* resistance at frequencies up to $1\,\text{kHz}$ [39]. Depending on the line length (e.g., by varying χ), this negative resistance may form an unstable RLC resonant circuit with line parasitics and reactive elements of filters [40]. The "addition" in series of the virtual impedance in GFL-C, GFL-P, and GFM implementations mitigates the possible adverse effects of the negative resistance, ensuring a broader stability margin (i.e., instability occurs at higher values of χ). Moreover, the addition of the virtual impedance is beneficial also because it lowers the gain of the unwanted PLL loop that closes at the PCC, which was mentioned in the introduction [10].
- The GFL-C CIG is stable in less cases than the GFL-P one because of its different way of implementing the *p/q control block*. This feature was already discussed and detailed in Sections III-A and III-B through Fig. 4 and 5. Through our implementation, the GFL-P CIG emulates better than the GFL-C one the behaviour of a synchronous generator — the always stable configuration in Table I.

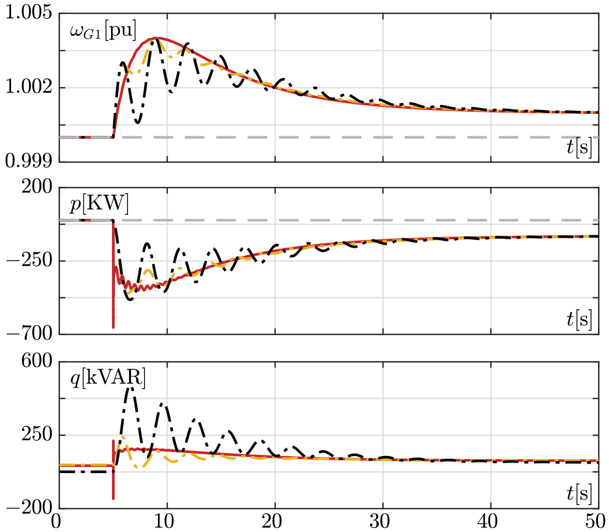

Fig. 7. Simulation results of the simple power grid in Fig. 6 in the **dynamic** sub-case of Table I. In all panels, the **red**, **yellow**, and **black** traces correspond to the GFL-P/$\chi_{\mathbf{1}}$, GFL-P/$\chi_{\mathbf{30}}$, and SYN/$\chi_{\mathbf{30}}$ cases, respectively. Upper panel: rotor speed ([pu]) of the G_1 synchronous generator (the dashed **gray** line denotes nominal speed). Second and third panels from top: C_1 p active power and q reactive power exchange. (the dashed **gray** line denotes C_1 active power set-point before the disturbance).

- The GFM CIG is unstable only in one more case than the GFL-P counterpart, that is, in the $\chi_{\mathbf{30}}$ one. Even in this case the GFM shows negative resistance that builds an unstable RLC resonating circuit. As said the onset of instability depends on several parameters and control block implementations. Thus this local worst behaviour of the GFM with respect to the GFL-P can be considered as "test case dependent".

2) Virtual inertia and damping provision: to show how the GFL-P supplies virtual inertia and damping, we report in Fig. 7 some results of the transient stability analyses obtained in the GFL-P/$\chi_{\mathbf{1}}$, GFL-P/$\chi_{\mathbf{30}}$, and SYN/$\chi_{\mathbf{30}}$ *stable* working conditions mentioned in Table I.

The comparison between the **yellow** and **black** traces in the upper panel highlights that, for the same line length (i.e., $\chi = 30$), the CIG of GFL-P kind (**yellow** trace) performs better than when it is replaced by a synchronous generator (**black** trace), since it grants reduced oscillations in the rotor speed of the G_1 synchronous generator.

The middle and bottom panels depict the C_1 CIG active and reactive power exchange triggered by the load step variation. The comparison between the **red** and **yellow** traces (which refer to the GFL-P case with χ=1 and χ=30, respectively) show that changes in L_{n2} line length leads to marginal differences in the proposed GFL CIG behaviour up to the occurrence of instability (with $\chi > 30$). In other words, the active power required from the CIG to support system frequency after the load step-change is exchanged regardless of L_{n2} line length.

B. A more complex power system

The second grid we considered is a modified version of the IEEE 9-bus 3-generator power system benchmark (WECC9B3G) used in [27]. We simulated it in two scenarios.

---

[13] This is because the ratio between the rated power of the G_1 generator and the C_1 CIG is 6. Furthermore, when C_1 is connected at bus_1 only the (small) internal equivalent impedance of G_1 limits the short-circuit current. When the CIG is connected to bus_2 or bus_3 (and $\chi = 1$), the SCR is still high because the $50/60\,\text{Hz}$ impedance of the L_{n1} and L_{n2} line is small.

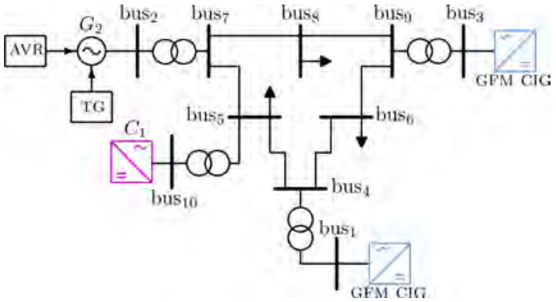

Fig. 8. The schematic of the IEEE 9-bus 3-generator (WECC9B3G) grid. AVR and TG respectively denote the automatic voltage regulator and turbine governor added to the synchronous generator G_2. Except for the C_1 CIG (**magenta**) and GFM CIGs (**blue**), the grid component models and related parameters are those of the PSAT distribution [36].

In the first scenario, we (i) used dynamic model of lines, transformers, and loads; (ii) added the TG turbine governor to the G_2 synchronous generator; and (iii) replaced the G1 and G3 synchronous generators with GFM CIGs given by the same (virtual) inertia and damping. Lastly, (iv) we connected the C_1 CIG through a transformer at bus_5. To not alter the PF solution of the original grid, the set-points of C_1 are $p^* = q^* = 0$, while those of the two GFM CIGs are the same of the G1 and G3 synchronous generators. Figure 8 depicts the grid simulated in this case. In the original grid (with all the synchronous generators connected), the inertia of the center of inertia (COI) was 11.016 s. After synchronous generator decommissioning, the COI inertia (exclusively contributed by G2) is 3.01 s. In this first scenario, the penetration level of GFM CIGs is 73%: this value refers to the percentage of the active power generated by the GFM CIGs relative to the total one generated in the system.

As in the previous subsection we considered the GFL-I, GFL-C, GFL-P, GFM and SYN types for C_1. According to the eigenvalue analyses, the system is unstable when the GFL-I and GFL-C are employed if dynamic models of lines, transformers and loads are used, regardless of the bus the C_1 CIG is connected to. Stability is restored only if algebraic models are used instead. On the contrary, when GFL-P, GFM, or SYN are used, the system is always stable independently from the line, transformer, and load model used.

Figure 9 includes some simulation results, obtained in the first scenario when GFL-P, GFM and SYN are used, by simulating at 20 s a +10% step variation of the active and reactive power of the load at bus_8. The **blue** traces refer to the results obtained without frequency support services provided by the C_1 CIG. We consider this as the reference case: through its comparison, we can highlight the benefits introduced by virtual inertia and damping provision from the proposed GFL CIG implementation (**red** traces, GFL-P case) and also compare it with that of a GFM CIG (**green** traces) and a synchronous generator replaced in its stead (**black** traces, SYN case).

The upper panel of Fig. 9 depicts the rotor speed of the single G_2 synchronous generator in each case. Without frequency support from the C_1 CIG, the rotor speed (**blue** trace) exhibits a nadir of about $0.993\,[\mathrm{pu}]$ at about 26 s (6 s after the power imbalance), and then slowly settles to about $0.9985\,[\mathrm{pu}]$ thanks to generator damping and the (delayed) mechanical power increment by the TG turbine governor. Additional inertia and damping provision, either through the proposed GFL CIG implementation (**red** trace) or an equivalent synchronous generator (**black** trace) or possibly a GFM CIG (**green** trace), largely decreases frequency deviations, thus limiting the frequency nadir. We can appreciate the large reduction of the ROCOF due to the virtual inertia contributed by C_1. The strong similarity between the **red** and **black** traces (which almost overlap) confirms that the GFL-P CIG properly emulates the behaviour of a synchronous generator.

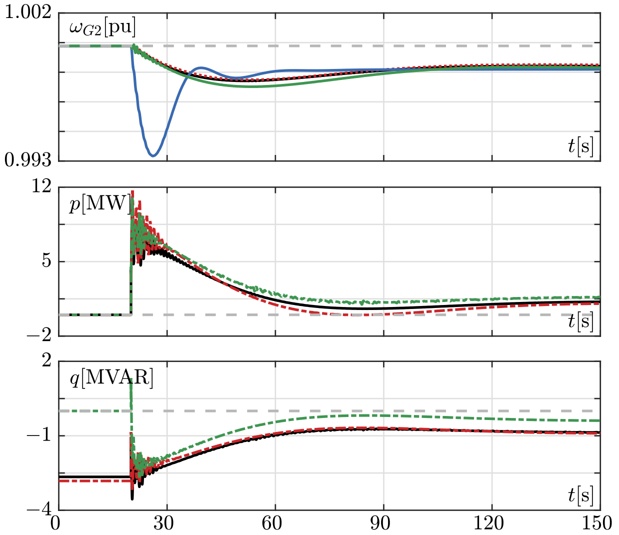

Fig. 9. Simulation results of the modified WECC9B3G grid in Fig. 8. The **blue** trace is obtained without C_1 CIG, while the **red**, **black** and **green** traces refer to the GFL-P, SYN and GFM cases, respectively. Upper panel: rotor speed ([pu]) of the G_2 synchronous generator (the dashed **gray** line denotes nominal speed). Middle and bottom panel: C_1 p and q power exchange (the dashed **gray** lines denote the C_1 power set-points before the disturbance).

This similarity can be observed also in the middle panel, which shows the active power exchange by C_1. Indeed, the **red** and **black** traces vary similarly after the load step-change and both show fast oscillations around 20 s, which are due to the fact that not all the electrical modes of the WECC9B3G system are well damped. The bottom panel reports the reactive power exchange by C_1 CIG in the GFL-P, GFM, and SYN scenarios. By looking at the middle and bottom panel, one can notice that in all the scenarios the C_1 CIG reacts to the load step-change by simultaneously varying both its active and reactive power, as a real synchronous generator does. An analogous behaviour is observed in the middle and bottom panels of Fig. 7.

In the second scenario, we also substituted G_2 with a GFM CIG and assigned the steady-state gain of the (removed) TG turbine governor to its power versus frequency droop controller: this ensures that, by applying the power imbalance of the first scenario, the systems frequency restores to the same steady state value. It is worth noting that in this case the penetration level of GFM CIGs is 100%.

The eigenvalue analyses, performed as in the first scenario, lead to the same conclusions. As to time-domain analyses, we applied the previous load step-change and obtained the results in Fig. 10. Compared to Fig. 9, we note a very similar behaviour, except for an almost sudden drop to the steady-

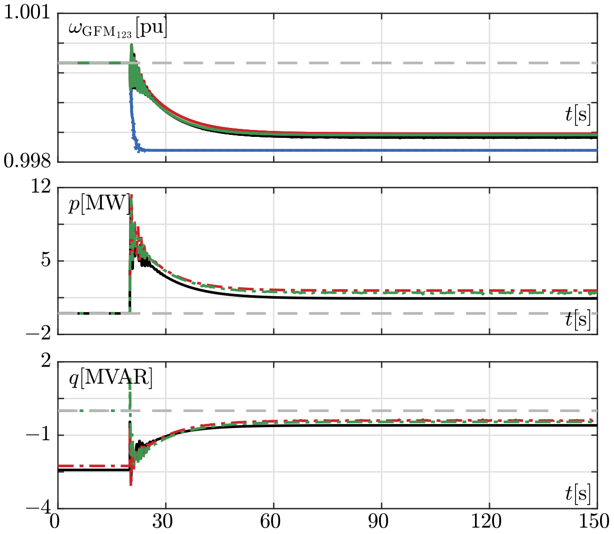

Fig. 10. Simulation results of the modified WECC9B3G grid in Fig. 8 by substituting also G_2 with a GFM CIG. Refer to the caption of Fig. 9 for the meaning of the colors of the traces in the panels. Upper panel: virtual rotor speeds ([pu]) of the 3 GFMs (the dashed gray line denotes nominal speed). Middle and bottom panel: C_1 p and q power exchange (the dashed gray lines denote the C_1 power set-points before the disturbance).

state value of the system frequency in the upper panel. This is due to a much faster action of the droop control of the GFM replacing G_2, which causes the disappearance of the nadir.

VI. CONCLUSIONS

In this paper, we proposed a new GFL CIG implementation (GFL-P) operating as voltage source. Compared to CIGs operating as a current source (GFL-I) and GFL-C CIGs, it is stable for a larger range of line lengths (i.e. strengths) despite using the same model of PLL. In particular, it is still stable with strong connections contrary to its GFL-C counterpart [18]: stability is also achieved by lowering the κ_p^{pll} and κ_p^{pll} parameters of the GFL-P CIG up to two magnitude orders. The main difference between the GFL-C and GFL-P implementations lies in how the virtual impedance block is used. In the GFL-C case, the inputs of this block are such that both the voltage magnitude and phase of the equivalent source emulated by the CIG are possibly changed following a frequency disturbance. On the contrary, in the GFL-P case, only the phase is changed, as happens when a synchronous generator reacts to deviations in grid frequency. To compute the phase, the structure itself of the synchronous generator, replicated through the virtual impedance block, is exploited. In the light of the above, the proposed implementation not only grants a higher stability margin than the conventional one, but also better emulates the behaviour of synchronous generators.

APPENDIX A
THE PHASE LOCKED LOOP (PLL)

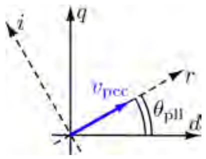

Fig. 11. The rotation from the (r,i) global to the (d,q) internal reference frame performed by the PLL by aligning the $v_{\mathrm{pcc}} = (v_{r,o}, v_{i,o})$ voltage vector at the PCC of the GFL CIG in Fig. 1(b) to the d-axis.

The design of PLL is a critical aspect since it deeply impacts on the stability of GFL CIGs [10], [27], [41]. The PLL model used in this paper is the following:

$$\begin{cases} \xi_q = \Omega_{\mathrm{lp}} \left(\dfrac{v_{q,o}}{\sqrt{v_r^2 + v_i^2}} - \widehat{v}_{q,o}^{\mathrm{pll}} \right) \\ \dfrac{d\,\widehat{v}_{q,o}^{\mathrm{pll}}}{dt} = \xi_q \\ \xi_\omega = \kappa_{\mathrm{p}}^{\mathrm{pll}} \xi_q + \kappa_{\mathrm{i}}^{\mathrm{pll}}\, \widehat{v}_{q,o}^{\mathrm{pll}} \\ \dfrac{d\delta_{\omega_{\mathrm{pll}}}}{dt} = \xi_\omega \\ \dfrac{d\theta_{\mathrm{pll}}}{dt} = \Omega_b \delta_{\omega_{\mathrm{pll}}} \\ \omega_{\mathrm{pll}} = \Omega_{\mathrm{ref}} + \delta_{\omega_{\mathrm{pll}}} . \end{cases} \tag{13}$$

The PLL regulates the θ_{pll} phase angle used in the "ri/dq" and "dq/ri" blocks in Fig. 1(e)-(g) so that $\xi_q = 0$. Considering Fig. 11, this implies that, when the $v_{\{r,i\},o}$ voltage vector at the PCC in the global reference frame is transformed (i.e., rotated) into $v_{\{d,q\},o}$ in the internal reference frame, it is aligned on the d-axis (i.e., $v_{q,o} = 0$).

ω_{pll} [pu] is the electrical angular frequency at the PCC estimated by the PLL, $\delta_{\omega_{\mathrm{pll}}}$[pu] is its variation with respect to the Ω_{ref} [pu] the system frequency, and ξ_ω [pu] is its derivative (i.e., the ROCOF). Ω_b is the system frequency (physical value), in general equal to $2\pi 50$ or $2\pi 60\,\mathrm{rad/s}$. Ω_{lp} is the cut-off frequency of the low pass filter and κ_p^{pll}, κ_i^{pll} are the proportional and integral gains of the PI controller of the PLL.

APPENDIX B
THE DEFAULT VALUES OF PARAMETERS OF THE GFL CIG

TABLE II
PARAMETERS OF THE GFL-C AND GFL-P CIGS.

$\kappa_{\mathrm{p}}^{\mathrm{pll}}$	200	$\kappa_{\mathrm{i}}^{\mathrm{pll}}$	300	Ω_b	100π [rad/s]
V_{ref}	10k [V]	κ_d	10	Ω_{ref}	1
P_{ref}	100 M [W]	κ_{si}	500	Ω_{lp}	500 [rad/s]
r_V	0.01	l_V	100 μ	κ_{pv}	200
κ_{iv}	100	c_F	0.2 m	l_F	80 μ
r_F	30 μ	κ_{ffi}	1	κ_{ad}	0.5
κ_{pc}	10	κ_{ic}	1000	κ_{ffv}	1
κ_{p}	0.03	κ_{q}	0	Ω_{F}	1000 [rad/s]
κ_{i}	1	κ_{pp}	1k	κ_{pi}	10k
ω_{ad}	50	p^*	0	q^*	0

Refer to [8] for the meaning of some parameters not described in this paper. If lacking a unit of measure, the parameters are in [pu].

REFERENCES

[1] U. Tamrakar, D. Shrestha, M. Maharjan, B. Bhattarai, T. Hansen, and R. Tonkoski, "Virtual Inertia: Current Trends and Future Directions," *Applied Sciences*, vol. 7, pp. 654–660, 2017.

[2] H.-P. Beck and R. Hesse, "Virtual synchronous machine," in *2007 9th International Conference on Electrical Power Quality and Utilisation*, 2007, pp. 1–6.

[3] S. D'Arco and J. A. Suul, "Equivalence of Virtual Synchronous Machines and Frequency-Droops for Converter-Based MicroGrids," *IEEE Trans. Smart Grid*, vol. 5, no. 1, pp. 394–395, Jan. 2014.

[4] S. D'Arco, J. A. Suul, and O. B. Fosso, "A Virtual Synchronous Machine implementation for distributed control of power converters in SmartGrids," *Electric Power Systems Research*, vol. 122, pp. 180–197, 2015.

[5] S. D'Arco and J. A. Suul, "Virtual synchronous machines — Classification of implementations and analysis of equivalence to droop controllers for microgrids," in *2013 IEEE Grenoble Conference*, 2013, pp. 1–7.

[6] W. Du, F. K. Tuffner, K. P. Schneider, R. H. Lasseter, J. Xie, Z. Chen, and B. Bhattarai, "Modeling of grid-forming and grid-following inverters for dynamic simulation of large-scale distribution systems," *IEEE Transactions on Power Delivery*, vol. 36, no. 4, pp. 2035–2045, 2021.

[7] B. Johnson, M. Rodriguez, M. Sinha, and S. Dhople, "Comparison of virtual oscillator and droop control," in *2017 IEEE 18th Workshop on Control and Modeling for Power Electronics (COMPEL)*, 2017, pp. 1–6.

[8] B. Barać, M. Krpan, T. Capuder, and I. Kuzle, "Modeling and initialization of a virtual synchronous machine for power system fundamental frequency simulations," *IEEE Access*, vol. 9, pp. 160 116–160 134, 2021.

[9] Y. Cheng, L. Fan, J. Rose, S.-H. Huang, J. Schmall, X. Wang, X. Xie, J. Shair, J. R. Ramamurthy, N. Modi, C. Li, C. Wang, S. Shah, B. Pal, Z. Miao, A. Isaacs, J. Mahseredjian, and J. Zhou, "Real-world subsynchronous oscillation events in power grids with high penetrations of inverter-based resources," *IEEE Trans. Power Syst.*, vol. 38, no. 1, pp. 316–330, 2023.

[10] D. Dong, B. Wen, D. Boroyevich, P. Mattavelli, and Y. Xue, "Analysis of phase-locked loop low-frequency stability in three-phase grid-connected power converters considering impedance interactions," *IEEE Transactions on Industrial Electronics*, vol. 62, no. 1, pp. 310–321, 2015.

[11] X. Fu, J. Sun, M. Huang, Z. Tian, H. Yan, H. H.-C. Iu, P. Hu, and X. Zha, "Large-Signal Stability of Grid-Forming and Grid-Following Controls in Voltage Source Converter: A Comparative Study," *IEEE Transactions on Power Electronics*, vol. 36, no. 7, pp. 7832–7840, 2021.

[12] Y. Zhou, H. Xin, D. Wu, F. Liu, Z. Li, G. Wang, H. Yuan, and P. Ju, "Small-Signal Stability Assessment of Heterogeneous Grid-Following Converter Power Systems Based on Grid Strength Analysis," *IEEE Transactions on Power Systems*, vol. 38, no. 3, pp. 2566–2579, 2023.

[13] W. Wenzong, M. H. Garng, R. Deepak, and F. Evangelos, "Transient stability analysis and stability margin evaluation of phase-locked loop synchronised converter-based generators," *IET Generation, Transmission And Distribution*, vol. 14, pp. 5000–5010(10), November 2020.

[14] L. Fan, Z. Miao, and D. Ramasubramanian, "Transient algebraic impedance derivations and applications for PLL-synchronized IBRs," *IEEE Transactions on Power Delivery*, vol. 39, no. 1, pp. 683–686, 2024.

[15] D. Pal and B. K. Panigrahi, "Reduced-order modeling and transient synchronization stability analysis of multiple heterogeneous grid-tied inverters," *IEEE Transactions on Power Delivery*, vol. 38, no. 2, pp. 1074–1085, 2023.

[16] M. M. Siraj Khan, Y. Lin, B. Johnson, M. Sinha, and S. Dhople, "Stability assessment of a system comprising a single machine and a virtual oscillator controlled inverter with scalable ratings," in *IECON 2018 - 44th Annual Conference of the IEEE Industrial Electronics Society*, 2018, pp. 4057–4062.

[17] Y. Lin, B. Johnson, V. Gevorgian, V. Purba, and S. Dhople, "Stability assessment of a system comprising a single machine and inverter with scalable ratings," in *2017 North American Power Symposium (NAPS)*, 2017, pp. 1–6.

[18] Y. Li, Y. Gu, and T. C. Green, "Revisiting grid-forming and grid-following inverters: A duality theory," *IEEE Trans. Power Syst.*, vol. 37, no. 6, pp. 4541–4554, 2022.

[19] "The new aggregated distributed energy resources (der_a) model for transmission planning studies: 2019 update," EPRI, Tech. Rep., 2019.

[20] D. Ramasubramanian, Z. Yu, R. Ayyanar, V. Vittal, and J. Undrill, "Converter Model for Representing Converter Interfaced Generation in Large Scale Grid Simulations," *IEEE Transactions on Power Systems*, vol. 32, no. 1, pp. 765–773, 2017.

[21] P. Kundur, N. Balu, and M. Lauby, *Power system stability and control*, ser. EPRI power system engineering series. McGraw-Hill, 1994.

[22] J. Rocabert, A. Luna, F. Blaabjerg, and P. Rodríguez, "Control of power converters in AC microgrids," *IEEE Transactions on Power Electronics*, vol. 27, no. 11, pp. 4734–4749, 2012.

[23] S. D'Arco, J. A. Suul, and O. B. Fosso, "Small-signal modeling and parametric sensitivity of a virtual synchronous machine in islanded operation," *International Journal of Electrical Power & Energy Systems*, vol. 72, pp. 3–15, 2015, the Special Issue for 18th Power Systems Computation Conference.

[24] X. Wang, Y. W. Li, F. Blaabjerg, and P. C. Loh, "Virtual-Impedance-Based Control for Voltage-Source and Current-Source Converters," *IEEE Transactions on Power Electronics*, vol. 30, no. 12, pp. 7019–7037, 2015.

[25] M. G. Taul, C. Wu, S.-F. Chou, and F. Blaabjerg, "Optimal Controller Design for Transient Stability Enhancement of Grid-Following Converters Under Weak-Grid Conditions," *IEEE Transactions on Power Electronics*, vol. 36, no. 9, pp. 10 251–10 264, 2021.

[26] D. Vilathgamuwa, P. Loh, and Y. Li, "Protection of microgrids during utility voltage sags," *IEEE Transactions on Industrial Electronics*, vol. 53, no. 5, pp. 1427–1436, 2006.

[27] Z. Zhou, W. Wang, T. Lan, and G. M. Huang, "Dynamic performance evaluation of grid-following and grid-forming inverters for frequency support in low inertia transmission grids," in *2021 IEEE PES Innovative Smart Grid Technologies Europe (ISGT Europe)*, 2021, pp. 01–05.

[28] Working Group B4.57, "Guide for the Development of Models for HVDC Converters in a HVDC Grid," Cigré, Paris, France, Tech. Rep. V15, Tech. Rep., 2014.

[29] Nationalgrid, "Performance of phase-locked loop based converters," System Operability Framework, Tech. Rep., Dec. 2017. [Online]. Available: www.nationalgrideso.com/document/102876/download

[30] F. Li and J. Ma, "Stability studies of grid-forming and grid-following inverter penetrated systems with different external power system models," *IEEE Transactions on Power Delivery*, pp. 1–12, 2024.

[31] D. del Giudice, F. Bizzarri, S. Grillo, D. Linaro, and A. M. Brambilla, "Impact of passive-components' models on the stability assessment of inverter-dominated power grids," *Energies*, vol. 15, no. 17, 2022.

[32] ESIG, "Diagnosis and mitigation of observed oscillations in IBR-dominant power systems: a practical guide," Energy System Integration Group's, Tech. Rep., Ago. 2024. [Online]. Available: https://www.esig.energy/oscillations-guide

[33] F. Bizzarri, A. Brambilla, G. S. Gajani, and S. Banerjee, "Simulation of Real World Circuits: Extending Conventional Analysis Methods to Circuits Described by Heterogeneous Languages," *IEEE Circuits and Systems Magazine*, vol. 14, no. 4, pp. 51–70, Fourthquarter 2014.

[34] F. Bizzarri and A. Brambilla, "PAN and MPanSuite: Simulation Vehicles towards the Analysis and Design of Heterogeneous Mixed Electrical Systems," in *NGCAS*. IEEE, 2017, pp. 1–4.

[35] D. Linaro, D. del Giudice, F. Bizzarri, and A. Brambilla, "PanSuite: A free simulation environment for the analysis of hybrid electrical power systems," *Electric Power Systems Research*, vol. 212, p. 108354, 2022.

[36] F. Milano, "A Python-based software tool for power system analysis," in *Procs. of the IEEE PES General Meeting*, Vancouver, BC, Jul. 2013.

[37] "Short-circuit modeling and system strength white paper," NERC, Tech. Rep., Feb. 2018.

[38] O. Damanik, O. C. Sakinci, G. Grdenić, and J. Beerten, "Evaluation of the use of short-circuit ratio as a system strength indicator in converter-dominated power systems," in *2022 IEEE PES Innovative Smart Grid Technologies Conference Europe (ISGT-Europe)*, 2022, pp. 1–5.

[39] D. del Giudice, A. Brambilla, D. Linaro, and F. Bizzarri, "Modular multilevel converter impedance computation based on periodic small-signal analysis and vector fitting," *IEEE Transactions on Circuits and Systems I: Regular Papers*, vol. 69, no. 4, pp. 1832–1842, 2022.

[40] F. Bizzarri, D. del Giudice, D. Linaro, and A. Brambilla, "An impedance method for stability analysis of power systems with large penetration of inverter based resources," in *2023 IEEE International Symposium on Circuits and Systems (ISCAS)*, 2023, pp. 1–5.

[41] J. Chen, W. Si, M. Liu, and F. Milano, "On the impact of the grid on the synchronization stability of grid-following converters," *IEEE Transactions on Power Systems*, vol. 38, no. 5, pp. 4970–4973, 2023.